Circumnuclear Rings and Lindblad Resonances in Spiral Galaxies

E. O. Schmidt[1,2,3], D. Mast[1,3,5] , R. J. Díaz[1,3,4], M. P. Agüero[1,3], G. Günthardt[1] , G. Gimeno[4], G. Oio[1,2,3], and G. Gaspar[1,3]

[1] Universidad Nacional Córdoba. Observatorio Astronómico de Córdoba. Córdoba, Argentina; eduschmidt@oac.unc.edu.ar
[2] Instituto de Astronomía Teórica y Experimental (IATE). Córdoba, Argentina
[3] Consejo de Investigaciones Científicas y Técnicas de la República Argentina, Avda. Rivadavia 1917, C1033AAJ, CABA, Argentina
[4] Gemini Observatory, 950 N Cherry Ave., Tucson, AZ 85719, USA
Received 2019 April 10; revised 2019 June 7; accepted 2019 June 8; published 2019 July 17

Abstract

In order to study the location of circumnuclear rings (CNR) and their possible relation with the inner Lindblad resonances (ILR), we investigate a sample of spiral galaxies. For this purpose, we have obtained and analyzed medium resolution spectra of five spiral galaxies in the range 6200–6900 Å. Through the Hα emission line, we constructed the radial velocity curves, and then the rotation curves. By fitting them, considering two or three components of an axisymmetric Miyamoto–Nagai gravitational potential, we constructed the angular velocity and Lindblad curves. In addition, we determined the CNR radius using the 2D spectra and generating the Hα spatial emission radial profiles. We determined the position of the resonances and we calculated the angular velocity pattern, which are in the range of 26–$47 \, \mathrm{km \, s^{-1} \, kpc^{-1}}$ for the galaxies of the sample. According to our results, the CNR are located between the inner ILR (iILR) and the outer ILR (oILR), or between the center of the galaxy and the ILR, when the object has only one of such resonance, in agreement with previous results. In addition, we calculated the dimensionless parameter defined as $\mathcal{R} = R_{\mathrm{CR}}/R_{\mathrm{bar}}$, being in the range 1.1–1.6, in agreement with previous results found in the literature.

Key words: galaxies: active – galaxies: kinematics and dynamics – galaxies: spiral

1. Introduction

The scientific community widely accepts the accretion of gas to the central supermassive black hole as the cause of nuclear activity in galaxies. These black holes would be a common component in most galaxies with a sufficiently massive bulge (e.g., Ferrarese & Ford 2005). However, only half (about 43%) of the local universe galaxies host active galactic nuclei (AGNs), as was suggested by Ho et al. (1997). This discrepancy between the presence of the supermassive black holes and nuclear activity must be studied in relation to the possibility and efficiency of transporting gas to the central region of the galaxy.

Circumnuclear rings (CNR) have radii ranging from 50 pc to 2 kpc and would be in the central regions of almost 20% of disk galaxies in the local universe with a local density of $0.54 \pm 0.12 \, \mathrm{galaxies \, Mpc^{-3}}$ (Díaz et al. 2004; Knapen 2005; Comerón et al. 2010). CNR act as repositories of gas, slowing the flow of gas toward the center, and have a strong star formation, reaching in some cases more than 50 times the star formation rate of a galactic disk (Kennicutt 1998). Depending on the duration of the ring, they may be responsible for the creation of an important stellar mass in the central regions (Van Der Laan et al. 2012).

The increase of nuclear activity in disk galaxies, whether in the form of starburst or AGN, seems to be closely linked to the evolution of the galaxy. It has been observed that both forms of activity coexist (e.g., Heckman et al. 1997) and are a clear manifestation of the symbiotic evolution of the galactic centers and their host galaxies. The close correlation observed between the masses of central black holes and the velocity dispersion of

stars in bulges (Ferrarese & Ford 2005) provides direct evidence of this evolution and allows for the study of the structure, dynamics, and evolution of the galaxies. At the same time, it is found that the kinematics of the gas clouds in the nucleus of the AGN is strongly influenced by the presence of the central black hole (e.g., Merritt & Ferrarese 2001; Tremaine et al. 2002; Schmidt et al. 2016, 2018; Schmidt 2019).

To boost and fuel the nuclear activity in the AGN or the nuclear starburst, there must be efficient gas conduction to the core. This process must be accompanied by a substantial loss of angular momentum of the gaseous material by almost eight orders of magnitude. This suggests the existence of gravitational torques that act through bars or interactions of galaxies. The nonaxysmmetric nature of the mass distribution facilitates the loss of angular momentum in the infalling material (e.g., Shlosman et al. 1990; Combes 2001).

There are many doubts about what are the proper conditions of temperature, density, and dynamics that trigger nuclear activity, and what are the parameters that regulate the duration of these outbreaks. For example, in the galaxy NGC 1241 the presence of several perturbations was detected in scales of hundreds of parsecs linked to the CNR (Díaz et al. 2003). Some of these disturbances are good candidates to remove the angular momentum of the gas and feed the Seyfert 2 nucleus of this galaxy. This motivated the systematic search for the presence of nuclear activity in galaxies with CNR, which suggested that the appearance of rings in the central regions seems to be related to the intrinsic properties of host galaxies, with self-instabilities, minor fusions, or the capture of giant molecular clouds (e.g., Corbin 2000; Díaz et al. 2006; Mast et al. 2006). There is evidence that points to the CNR as tracers of the feeding of nuclear activity. Arsenault (1989) reported a higher incidence of the combination of bars and rings in starburst and AGN host galaxies, with respect to normal galaxies. On the other hand, Hunt & Malkan (1999) found that Seyfert galaxies

Table 1
Galaxy Sample

Galaxy (1)	R.A. (2)	Decl. (3)	D (Mpc) (4)	Scale (kpc arcsec^{-1}) (5)	mag. (6)
IC 1438	22:16:29.09	−21:25:50.5	34.7	0.168	11.57(∗)
IC 4214	13:17:42.69	−32:06:06.1	29.6	0.144	10.72(∗)[a]
NGC 1512	04:03:54.28	−43:20:55.9	10.2	0.050	11.13
NGC 2935	09:36:44.85	−21:07:41.3	28.3	0.137	11.92
NGC 6753	19:11:23.64	−57:02:58.4	42.5	0.206	11.74

Note.

[a] Column (1): target ID; column (2): R.A. (J2000); column (3): Decl. (J2000); column (4): distance in megaparsecs; column (5): scale in kiloparsec arcsec^{-1}; column (6): R-band calibrated magnitude (Doyle et al. 2005); (∗) R (Cousins); (R_T) magnitude (Lauberts & Valentijn 1989).

have more rings (interior and exterior) than normal galaxies. The study by Agüero et al. (2016) suggests a simultaneity between Seyfert activity and CNR greater than that expected for the morphological type distribution of host galaxies. The ratio between Seyfert 2/Seyfert 1 with CNR would be, according to these authors, three times greater than expected considering galaxies without rings, in opposition to the ratio that predicts the geometric paradigm of the classic unified model for AGN.

The preferred position of the rings with respect to the resonances in the disks of the galaxies is an open problem, which also motivates our work. According to the most accepted theory, the CNR are formed close to the inner Lindblad resonances (ILR; Lindblad 1964) when the gas loses angular momentum and accumulates in that region (e.g., Shlosman et al. 1990; Knapen et al. 1995; Combes 1996; Comerón et al. 2010; Piñol-Ferrer et al. 2014). It was suggested that CNR are formed between the center and the ILR, when there is only one of such resonance, or between the inner ILR (iILR) and the outer ILR (oILR) when there are two resonances (e.g., Combes 1996). In this context, CNR form because of resonant interactions of the gas with the inner resonances. Related to this, the bar torque changes its sign when it crosses each ILR. For example, in the case of only one ILR, the gas inside (outside) the resonance receives a positive (negative) torque and then it moves outward (inward).

On the contrary, some authors argue that ring formation is not due to resonances but by the centrifugal barrier, which the inflowing gas along dust lanes cannot overcome (e.g., Kim et al. 2012a, 2012b; Seo & Kim 2014; Li et al. 2015). In this scenario, the formation and location of the rings are not directly determined by the ILR and there would be no direct connection between them (e.g., Kim et al. 2012b; Ma et al. 2018). From hydrodynamic numerical simulations it is shown that the presence of x2 orbits is the requirement for the formation of CNR and that there are no internal Lindblad resonances in barred galaxies (Regan & Teuben 2003). Li et al. (2015) suggest that knowing the radius of the ILR would be insufficient to find the location of the CNR.

Comerón et al. (2010) studied the sizes and shapes of CNR in a sample of more than 100 galaxies and they found that objects with stronger bars host smaller rings. According to them, the ring ellipticity is in the range of 0–0.4. It was reported that the size of the rings is well correlated with the galaxy mass distribution (Mazzuca et al. 2011). According to these authors, a higher mass concentration results in a smaller ring. They also found that the CNR size is dependent on the bar strength, in agreement with recent results of Seo et al. (2019).

In the present work we study a sample of five galaxies with CNR reported in the literature using long-slit optical spectra to provide elements that allow us to shed light on the dynamic nexus between CNR and nuclear feeding mechanisms. In particular we studied the CNR position and their relation with Lindblad resonances. This paper is structured as follows. Section 2 introduces the observed sample and briefly describes the observations, Section 3 presents the complete kinematical analysis, and Section 4 offers a discussion of the obtained results. Finally, Section 5 provides a brief summary of the work and the conclusions.

2. Sample and Observations

For the present work, we selected a subsample of five spiral galaxies from a mother sample of nearby galaxies with CNR, observable from the southern hemisphere and with spatial scales that allow us to resolve the rings with 2–4 m class telescopes. Table 1 lists the main properties that characterize the galaxies, such as the object name, R.A., decl., distance, scale, and apparent magnitude in the R filter. The data were taken from the Nasa Extragalactic Database (NED).[6]

Observations were performed in different campaigns between 2002 and 2004 using the REOSC spectrograph at the 2.15 m telescope of the Complejo AStronómico el LEOncito (CASLEO), in Argentina. All spectra were taken in the long-slit mode. The detector is a Tektronix 1024 × 1024 CCD with 24 μm pixels. We used a 1200 line mm^{-1} grating giving a spectral resolution of ∼3500 in the range of 6200–6900 Å. The dispersion was 32 Å/mm^{-1}, the reciprocal dispersion 0.76 Å pixel^{-1}, the angular scale 1″02 pixel^{-1}, and the spectral resolution 1.9 Å. The average seeing during the observations was ∼2″5. The standard procedure was followed for the observations and data reduction, including correction for bias, dark current, and flat field. The spectra were wavelength calibrated using comparison lines from a Cu-Ne-Ar lamp and three standard stars were observed each night to flux calibrate the spectra. Data reduction was carried out using the Image Reduction and Analysis Facility (IRAF)[7] reduction package. Additional observational information can be found in Mast et al. (2005).
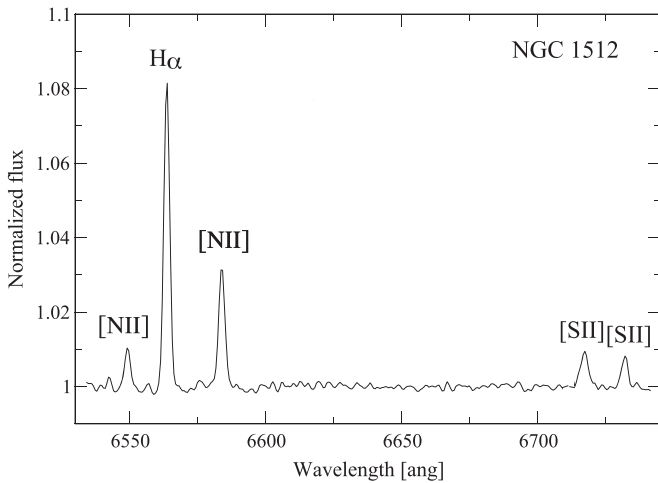
Figure 1. Rest-frame NGC 1512 sample spectrum with the main emission lines indicated.

3. Analysis

3.1. Radial Velocity Curves

Once the spectra were reduced, we proceeded to make extractions using one pixel wide apertures along the slit, covering the entire spatial range with $H\alpha$ emission. Figure 1 shows one of these extractions, as an example, for the galaxy NGC 1512. This spectrum depicts the more conspicuous emission lines at this wavelength range, i.e., $H\alpha\lambda6563$, [N II] $\lambda\lambda6548,6584$, and [S II]$\lambda\lambda6713,6731$.

Using the IRAF task *splot*, we fitted gaussians to each emission line to determine its parameters: intensity, FWHM, flux, and centroid. In the present work we will focus on the kinematical study derived from $H\alpha$. Once radial velocities of each extracted spectrum have been determined, we constructed the radial velocity curves for each galaxy. On Table 2 we summarized the main properties of the curves. Images of the galaxies, the location of the slit, and the radial velocity curves are shown in Figure 2. The adopted systemic radial velocity (V_{syst}) for each galaxy are $2621 \, km \, s^{-1}$ for IC 1438, $2330 \, km \, s^{-1}$ for IC 4214, $924 \, km \, s^{-1}$ for NGC 1512, $2271 \, km \, s^{-1}$ for NGC 2935, and $3160 \, km \, s^{-1}$ for NGC 6753. These velocities are the ones that better symmetrize the radial velocity curves and they are in agreement with values found in the literature. For IC 4214 and NGC 2935, V_{syst} does not coincide with V_{obs} at the continuum peak, so an offset has to be applied to symmetrize the radial velocity curves. This offset, nevertheless, is always a fraction of the resolution element ($\sim 1''$) and we do not have enough spatial information to make conjectures about the possible off-centered nucleus, although we do not discard this possibility. The uncertainties in the radial velocities were calculated using the formula presented in Keel (1996).

All radial velocity curves are relatively smooth, with the exception of NGC 2935, which deviates from circular rotation around the galaxy center from ~ 1 to 3 kpc on the red side of the curve.

3.2. Rotation Curves and Resonances

In order to determine the rotation curves of the galaxies, we calculated the inclination angle of each object. Through isophotal fitting to digitized sky survey (DSS)[8] R-band images,

---

8 The online digitized sky surveys server at the ESO Archive.

Table 2
Radial Velocity Curve Properties

Galaxy	Central Gradient (km s^{-1} arcsec^{-1})	Vr max. (km s^{-1})	$r_{Vr\mathrm{max}}$ (arcsec)
(1)	(2)	(3)	(4)
IC 1438	17	83	5
IC 4214	24	210	9
NGC 1512	9	140	13
NGC 2935	4	90	45
NGC 6753	17	193	12

Note. Column (1): target ID; column (2): radial velocity gradient in the inner part of the curve, determined between both velocity maxima; column (3): maximum velocity reached by the curve; column (4): position where the maximum is reached.

we measured the major and minor axis of each galaxy and we calculated the inclination angle considering that $\cos i = \mathcal{B}/\mathcal{A}$, where $\mathcal{B}$ and $\mathcal{A}$ are the minor and major axis, respectively, of the outer isophote. We assumed the photometric position angle (P.A.$_{phot}$) as the angle measured from north to east of the outer isophote major axis. Once the inclination angle is obtained, and assuming that PA$_{phot}$ coincides with the kinematic P.A. (P.A.$_{kin}$), the circular rotation velocity can be calculated. After a small correction due to the difference between PA$_{obs}$ (position angle of the observation) and PA$_{kin}$, we are able to determine the circular velocity by

$$V_c = \frac{V_{obs} - V_{syst}}{\sin(i)}, \qquad (1)$$

where V_c is the circular velocity, V_{obs} is the observed radial velocity, and V_{syst} is the systemic radial velocity. While, in general, PA$_{kin}$ is defined as the mean value of the radial evolution of the kinematic PA, our adopted PA$_{phot} \sim$ PA$_{kin}$ was consistent with the values found in the literature for our objects.

We fitted the rotation curves of the galaxies considering two or three mass components, depending on the case, corresponding to axisymmetric Miyamoto–Nagai gravitational potentials (Miyamoto & Nagai 1975)

$$\Phi(R, z) = -\frac{GM}{\sqrt{R^2 + [a + \sqrt{z^2 + b^2}]^2}}, \qquad (2)$$

where Φ (R, z) is the Miyamoto–Nagai potential at (R, z) position, M is the total mass, and a and b are shape parameters. The ratio $b/a \sim 0.4$ corresponds to a flattened disk distribution, $b/a = 1$ to an ellipsoidal distribution, and $b/a \sim 5$ to a spherical distribution (e.g., Binney & Tremaine 1987).

The galaxies IC 4214, NGC 1512, NGC 2935, and NGC 6753 were fitted considering the presence of only two galactic subsystems (a central ellipsoidal component and a flattened disk) without the need for the external spherical component (halo). On the other hand, the IC 1438 rotation curve was fitted considering the presence of three galactic subsystems: a central ellipsoidal component, a flattened disk, and a massive halo.

Table 3 lists the obtained parameters that optimize the χ^2 minimization fit, such as the scale parameters and the total mass.
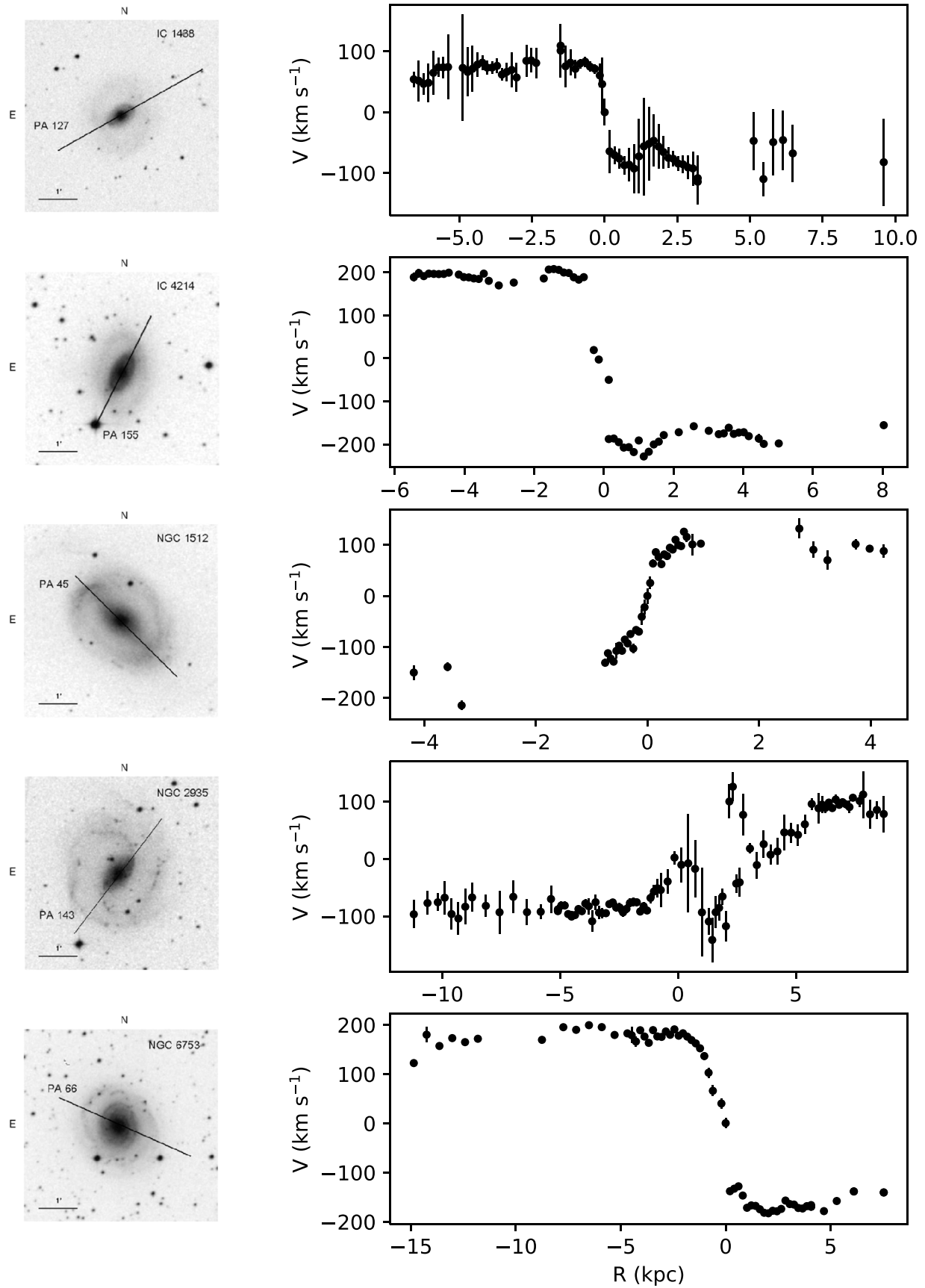
Figure 2. Left: galaxy images with the slit positions indicated. Right: Hα radial velocity curves of the observed galaxies. The error bars were determined using the formula of Keel (1996). Note that in some cases the size of the error bar is smaller than the size of the used symbol.

Table 3
Rotation Curve Parameters Considering the Fitted Miyamoto–Nagai Model

Galaxy	Component 1	Component 2	Component 3
IC 1438	$a_1 = 0.20$ kpc $b_1/a_1 = 1$ $M_1 = 5.6 \times 10^9\,M_\odot$	$a_2 = 1.50$ kpc $b_2/a_2 = 0.33$ $M_2 = 2.0 \times 10^{10}\,M_\odot$	$a_3 = 7.0$ kpc $b_3/a_3 = 1.43$ $M_3 = 2.1 \times 10^{11}\,M_\odot$
IC 4214	$a_1 = 0.25$ kpc $b_1/a_1 = 0.92$ $M_1 = 2.1 \times 10^{10}\,M_\odot$	$a_2 = 3.14$ kpc $b_2/a_2 = 0.63$ $M_2 = 1.4 \times 10^{11}\,M_\odot$	
NGC 1512	$a_1 = 0.20$ kpc $b_1/a_1 = 1$ $M_1 = 3.4 \times 10^9\,M_\odot$	$a_2 = 2.5$ kpc $b_2/a_2 = 0.20$ $M_2 = 2.7 \times 10^{11}\,M_\odot$	
NGC 2935	$a_1 = 0.50$ kpc $b_1/a_1 = 1$ $M_1 = 6.8 \times 10^9\,M_\odot$	$a_2 = 2.8$ kpc $b_2/a_2 = 0.61$ $M_2 = 3.6 \times 10^{10}\,M_\odot$	
NGC 6753	$a_1 = 0.68$ kpc $b_1/a_1 = 0.73$ $M_1 = 7.9 \times 10^{10}\,M_\odot$	$a_2 = 4.7$ kpc $b_2/a_2 = 0.49$ $M_2 = 3.4 \times 10^{11}\,M_\odot$	

Considering the potential, the circular velocity can be inferred as $V_c = \sqrt{-R(\partial\Phi/\partial R)}$ (see for example Binney & Tremaine 1987). Once the circular velocity has been obtained, the angular velocity can be easily calculated as $\Omega = V_c/R$ and the epicyclic frequency can be inferred (e.g., Elmegreen 1998) as

$$\kappa^2 = 4\Omega^2\left[1 + \frac{1}{2}\left(\frac{R}{\Omega}\frac{d\Omega}{dR}\right)\right]. \qquad (3)$$

The location of the ILR and outer Lindblad resonance (OLR) can be calculated taking into account that $\Omega - \Omega_p = -\kappa/2$ at OLR and $\Omega - \Omega_p = \kappa/2$ at ILR (e.g., Binney & Tremaine 1987; Elmegreen 1998), where Ω_p is the pattern speed. In addition, the location of the corotation resonance (CR) can be inferred when $\Omega = \Omega_p$.

In order to construct the Linblad $\Omega - \kappa/2$ and $\Omega + \kappa/2$ curves for the galaxies, the first thing we did was determine the position of the CR. There is more than one way to calculate the radius of this resonance. For example, in order to do this Puerari & Dottori (1997) presented a method based on the Fourier analysis of azimuthal profiles (Aguerri et al. 1998; Díaz et al. 2003). On the other hand, Prendergast (1983) suggested that the dust lanes indicate the location of the shock regions in the spiral arms. This interpretation was first quantified by Roberts et al. (1979). Inside the corotation radius, dust lanes are located in the trailing side of the bar or the spiral arms perturbation pattern. In these locations the gas in circular orbits in the disk encounters the perturbation pattern, which is moving at lower angular velocity. Outside the corotation radius it is expected that the dust lanes are in the leading side of the perturbation pattern. The radii in which the dust lanes change from the trailing to the leading side of the perturbation pattern, indicate the approximate location of the CR. Taking into account all these considerations, we determined the CR radius by measuring directly from DSS images.

Considering the measured length of the bar ($R_{\rm bar}$) and the corotation radius ($R_{\rm CR}$), the dimensionless parameter $\mathcal{R}$, defined as $\mathcal{R} = R_{\rm CR}/R_{\rm bar}$, is usually useful to characterize the bars as fast or slow. For the galaxies in our sample we obtained values for $\mathcal{R}$ in the range 1.1–1.6, in agreement with

previous results (e.g., Debattista & Sellwood 2000; Rautiainen et al. 2008; Aguerri et al. 2015; Guo et al. 2019).

The rotation curves corresponding to the fitted axial symmetric model are illustrated in the left panels of Figure 3, as well as the angular velocity curves and the Lindblad $\Omega - \kappa/2$ and $\Omega + \kappa/2$ curves (right panel) of the studied galaxies. Note that in all of the left panels of this figure, $V_{\rm circ}$ is 0 near the center. This is mostly likely due to limited resolution, taking into account that if there is a central mass concentration (e.g., a black hole), the rotation velocity should rise toward the center. The net effect of the finite spatial resolution is to average plus and minus values in both sides of nucleus along the major axis (Sofue 2013). The spectra have average spatial resolutions of $2\rlap{.}''5$, with a $1\rlap{.}''02$ spatial sampling. The innermost resolved rotation velocities are of the order of tens of km s^{-1} at radii of 100–300 pc, without a change of slope toward the galactic core. This means that the gravitational sphere of influence of the supermassive black hole is not resolved in the rotation curve for the average distance of the sample.

Table 4 lists where the different resonances of the studied galaxies are located (in units of kiloparsec), the pattern speed values, Ω_p (in units of km s^{-1} kpc^{-1}), the radial length of the bar (in units of arcsec and kiloparsec), and the dimensionless parameter $\mathcal{R}$.

3.3. Spatial Profiles

To determine the CNR radius, we used the 2D spectra and generated the Hα spatial emission radial profiles (Figure 4). As can be seen in Figure 4, we perform an extraction by joining the emission peaks. This direction is oblique to both the spatial and spectral directions, so it is then necessary to project the profile over the spatial direction to have the distance in arcsec. In this way we are using the dispersive capacity of the diffraction grating to separate the emission and to be able to resolve and measure the rings radii. Unfortunately, we only have the information in the direction of the slit, so the P.A. of the ring is unknown. Although it is possible to measure the P.A. of the CNR from images (e.g., Pogge 1989; Buta & Crocker 1993; Comerón et al. 2010), the discrepancy in both
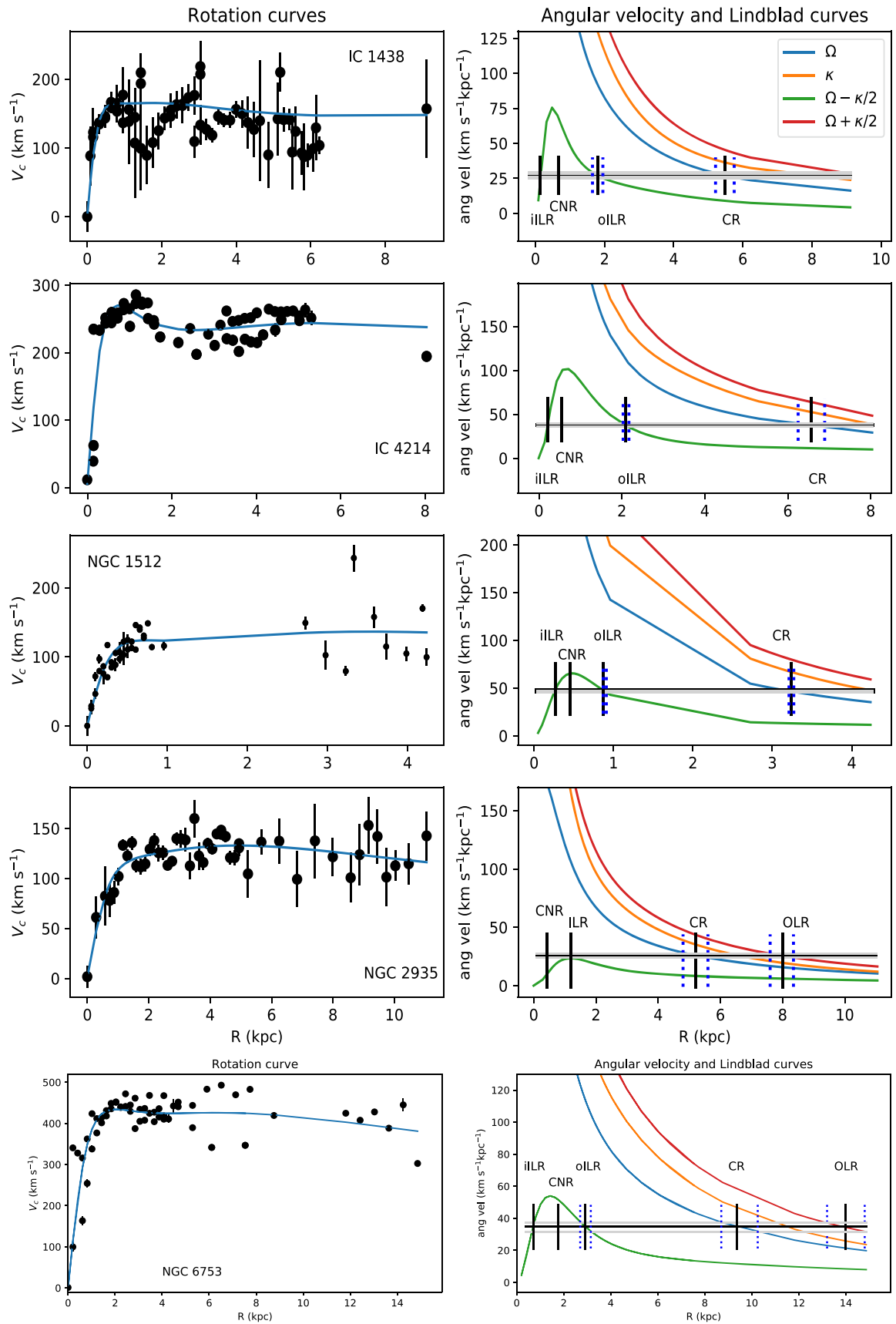
Figure 3. Left panels: rotation curves fitted with two or three components corresponding to axisymmetric Miyamoto–Nagai potential. In all cases, V_{circ} is 0 near the center. This is due to limited spatial resolution that makes the gravitational sphere of influence of the supermassive black hole not resolved in the rotation curves. Right panels: angular velocity curves and Lindblad curves, in units of km s^{-1} kpc^{-1}. The horizontal black and gray solid lines indicate the perturbation pattern angular velocity and its uncertainty. The vertical blue dotted lines show the uncertainties of the position of the resonances.

Table 4
Angular Velocity Pattern and Resonances

Galaxy	Ω_p (km s^{-1} kpc^{-1})	ILR (kpc)	CR (kpc)	OLR (kpc)	r_{bar} (arcsec)	R_{bar} (kpc)	$\mathcal{R}$
1	2	3	4	5	6	7	8
IC 1438	27 ± 2	iILR = 0.13–oILR = 1.8 ± 0.2	5.5 ± 0.3	⋯	20.6 ± 0.9	3.5 ± 0.1	1.6 ± 0.1
IC 4214	38 ± 2	iILR = 0.21–oILR = 2.1 ± 0.1	6.6 ± 0.3	⋯	28.6 ± 0.9	4.1 ± 0.1	1.6 ± 0.1
NGC 1512	47 ± 1	iILR = 0.26–oILR = 0.87 ± 0.05	3.2 ± 0.1	⋯	60 ± 4	3.0 ± 0.2	1.1 ± 0.1
NGC 2935	26 ± 2	1.2 ± 0.2	5.2 ± 0.4	8.0 ± 0.4	24.3 ± 0.7	3.3 ± 0.1	1.5 ± 0.2
NGC 6753	35 ± 3	iILR = 0.72–oILR = 2.9 ± 0.2	9.4 ± 0.8	14.0 ± 0.8	⋯	⋯	⋯

Note. Column 1: galaxy name; column 2: pattern angular velocity; column 3: position of the ILR; column 4: location of the CR; column 5: position of the OLR; column 6: radius of the bar in arcsec; column 7: radius of the bar in kiloparsec; column 8: the dimensionless parameter defined as $\mathcal{R} = R_{CR}/R_{bar}$.

P.A. and radius between different authors shows that it is not a simple task. In addition, in the case of spectra it is easier to correctly isolate the Hα emission to define the ring. Another question that requires a proper definition would be which point of the CNR range is considered its radius. For the present work we decided to measure the distance between the emission peaks on both sides. The nucleus of the galaxy is defined as the continuum emission peak in the Hα spectral region. In this way we avoid uncertainties due to diffuse emission in the internal or external region of the ring.

The CNR of the five galaxies studied in this paper have been previously measured in other works. As we will see below (Section 4), these measurements vary from one work to another. Most of these previous studies use images in different bands to determine the CNR radius, obtaining distinct values. For completeness and looking for consistency in the measurement criteria, we have performed our own determinations of the CNR radio through the Hα profiles (Figure 4). It should be noted that we have information only at the direction of the observed P.A. and this may differ from the actual P.A. of the CNR. In the comparison with the values from the literature we carried out in Section 4, these differences are considered.

4. Discussion

In this section we consider each galaxy separately, taking into account what was obtained in each one, and comparing in some cases with other results found in the literature. Then we will see how the obtained results fit or not within a particular scenario. Before getting into the analysis, it is important to make some considerations about the measured values.

The inclination angle of a galaxy, governed by the ratio of the semimajor and minor axis of the object, may vary with the distance to the center, as it may be the case of a warped disk (e.g., Bosma 1978; Briggs 1990; Reshetnikov & Combes 1999; Beckman et al. 2004; Saha et al. 2009; Buta et al. 2015). In addition, the P.A.$_{kin}$ may also vary with radius of the galaxy and may differ from the P.A.$_{phot}$. Taking all this into consideration, our assumption of a "perfect" disk may include some uncertainties, which are very difficult to quantify. However, when comparing with values from the literature and, where possible, showing the effects of possible variations in the measured quantities, we can see that our approximations are valid and provide solid results within the reported uncertainties.

Concerning the bar length, the measurement methods used in different works (Athanassoula & Misiriotis 2002) can yield values that differ by as much as a factor 2 (Comerón et al. 2010). For this reason, in the present work we have visually

measured the galaxy bar lengths (e.g., Kormendy 1979; Martin 1995; Hoyle et al. 2011) directly from Two Micron All-Sky Survey (2MASS) images, since it is in these images in the near-infrared where the contribution of the more evolved stellar population is greater, as well as the contrast with the gaseous disk, which allows us to better visualize the extent of the bar.

Determining the position of the CNR and its radius is not an easy task either. In this work we have measured the radius of the rings, as we said before, from the Hα profile. In the comparison with the values from the literature, our approach was to use our own measurement when the dispersion of values in the literature was very large. In all cases, the dispersion of measured values could give us an idea of the uncertainties involved in the determination of the CNR radius.

The uncertainties in the position of the resonances were determined by successive measurements of the CR (OLR in the case of NGC 6753) radii visually from DSS images and doing statistics. In this way we were able to take into account possible errors due to the determination of the center of the galaxy and asymmetries in the disk.

4.1. Notes on Individual Objects

IC 1438. According to Buta et al. (2009), it is a weakly barred galaxy with a faint outer ring and presents enhanced star formation in nuclear and inner rings. Through isophotal fitting to DSS *R*-band images, we measured an inclination angle of 32°, in agreement with previous results (e.g., Böker et al. 2008). The parameters of the fitted Miyamoto–Nagai components imply the presence of three galactic subsystems such as an intermediate bulge−disk, a disk, and an external halo, with a total mass of $2.4 \times 10^{11} M_\odot$. We measured a bar radial length of $20''6 \pm 0''9$, equivalent to (3.5 ± 0.1) kpc, in agreement with the value obtained by Comerón et al. (2010). We assumed that the CR is located at (5.5 ± 0.3) kpc from the center. Furthermore, this galaxy shows an angular velocity pattern of $\Omega_p = (27 \pm 2)$ km s^{-1} kpc^{-1}. Related to this, the dimensionless parameter $\mathcal{R}$ results 1.6 ± 0.1, consistent with a slow bar (e.g., Debattista & Sellwood 2000; Guo et al. 2019). According to the Hα profile (Figure 4), the CNR radius is $2''45$, equivalent to 0.41 kpc. However, other values are found in the literature. For example, Böker et al. (2008) obtained a CNR radius of 0.537 kpc with a P.A.$_{CNR}$ of 81°. In addition, according to Buta & Crocker (1993) and Comerón et al. (2010), the CNR semimajor axis is 0.650 kpc and 0.680 kpc, respectively. All these values show a dispersion of about 25% and it may be due to the different P.A.s considered. Assuming even the most extreme possible values, it can be said
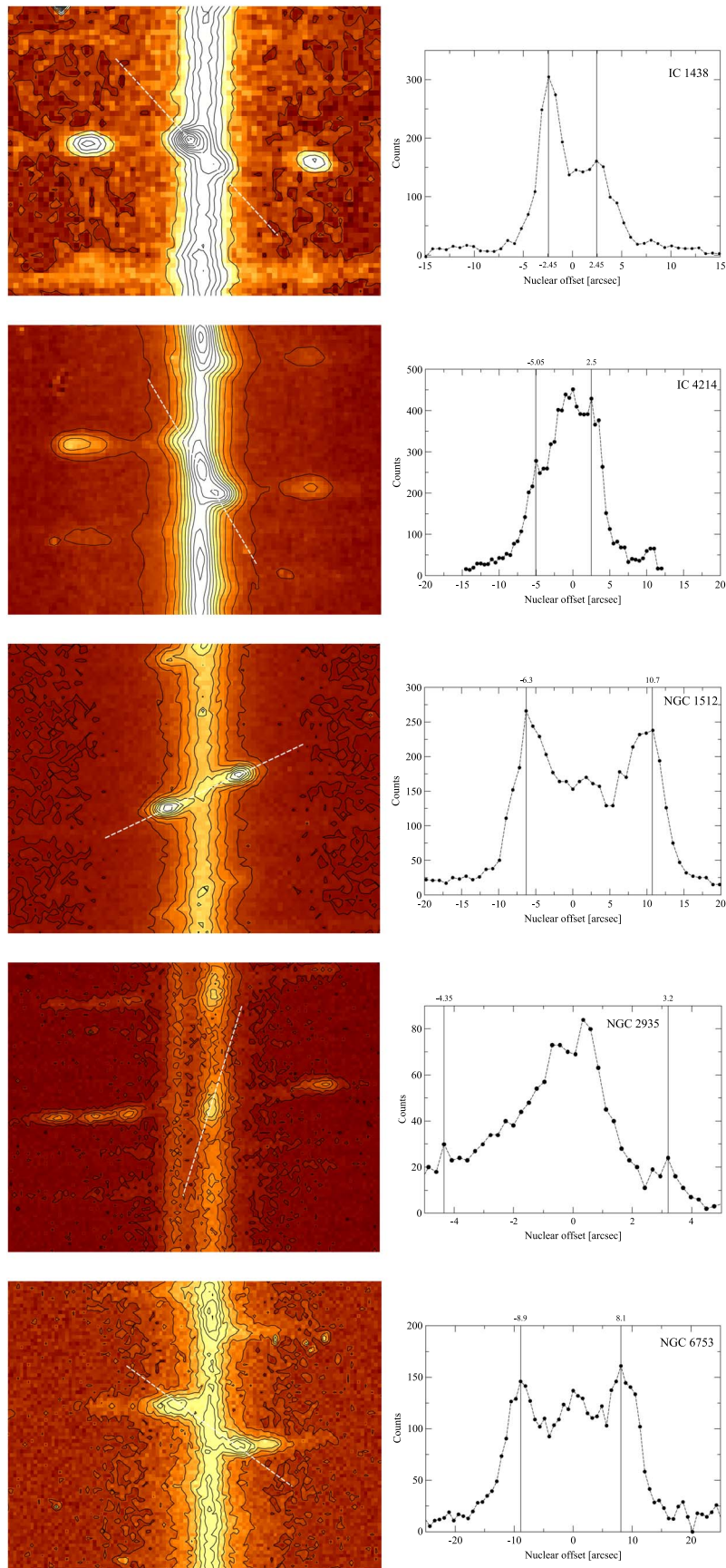
Figure 4. Left: zoom-in of the Hα region in the 2D observed spectra. The horizontal direction is the spatial coordinate while the vertical direction represents the wavelength coordinate ascending up. The white dotted line indicates the direction of the extraction in order to construct the radial profiles. Right: Hα radial profiles extracted from the 2D spectra in an oblique direction, and projected on the spatial direction. Vertical lines indicate the Hα peak intensities at both sides of the galaxy center, which we associate with the CNR.

that the CNR is located between the iILR (0.13 kpc) and the oILR (1.9 kpc). Our data does not allow us to have information about the location of the OLR, but it could be located at around 10 kpc from the center, considering the end of the spiral arms. On the other hand, our slit P.A. is 127°, in agreement with the NED reported P.A.$_{phot}$. However, Böker et al. (2008) consider a P.A. of 145° for this galaxy. This difference of 18° in P.A. would produce a negligible difference in the Ω_p value, and, as a consequence, in the location of the iILR, and a difference of 0.05 kpc in the location of the oILR.

IC 4214. It is a weakly barred galaxy (Moss et al. 1999) and according to the position of the galaxy in diagnostic diagrams based on line flux ratios, this object presents low-ionization nuclear emission line region (LINER) activity (Saraiva et al. 2001). These authors also report minimal star formation in the galaxy nucleus. Through isophotal fitting from DSS *R*-band images, we obtained an inclination angle of 54°, which is consistent with the value published by NED. The parameters of the fitted Miyamoto–Nagai components imply the presence of two galactic subsystems and a total mass of $1.6 \times 10^{11} M_\odot$. We measured a radial length bar of $R_{bar} = 28\rlap.{''}6 \pm 0\rlap.{''}9$, equivalent to (4.1 ± 0.1) kpc, which is in agreement with the value obtained by Comerón et al. (2010). We assumed that the CR is located at the end of the bar, at (6.6 ± 0.3) kpc from the center of the galaxy, with a dimensionless parameter of $\mathcal{R} = 1.6 \pm 0.1$. Furthermore, this object presents an angular velocity pattern of $\Omega_p = (38 \pm 2)$ km s^{-1} kpc^{-1}. It can be seen in Figure 4 that the CNR is located about 0.6 kpc $(3\rlap.{''}8)$ from the nucleus. According to Buta & Crocker (1993), the major axis of the ring is $0\rlap.{'}146$, equivalent to a semimajor axis of 0.632 kpc $(4\rlap.{''}38)$. Comerón et al. (2010) report a ring semimajor axis of $7\rlap.{''}6$, equivalent to 1.15 kpc. Despite the dispersion of reported values, and considering even the the extreme measurements, the CNR is located between the iILR (0.21 kpc) and the oILR (2.04 kpc). As in the previous case, we do not have any information about the location of the OLR. According to our measurements, the spiral arms seem to end at about $53\rlap.{''}7$ ($\sim$7.75 kpc) from the center of the galaxy.

NGC 1512. Through isophotal fitting from DSS *R*-band images, our measurements of the major and minor axis of the galaxy give an inclination angle of 54°, in agreement with other works (see NED). The rotation curve fitting considering two components of the Miyamoto–Nagai potential gives a total mass of $2.7 \times 10^{11} M_\odot$. According to our measurements, the bar has a total length of $2'$, equivalent to a radial length of $60'' \pm 4''$ and (3.0 ± 0.2) kpc. The CR was assumed to be at the end of the gap between the bar and the spiral arms, as mentioned before, at (3.2 ± 0.1) kpc from the galactic center. The system angular velocity pattern is $\Omega_p = (47 \pm 1)$ km s^{-1} kpc^{-1}. Related to this, the parameter $\mathcal{R}$ is 1.1 ± 0.1, consistent with a fast bar (Debattista & Sellwood 2000; Rautiainen et al. 2008; Guo et al. 2019). According to Ma et al. (2017), this galaxy has a nuclear ring with a total stellar mass of $\sim 10^7 M_\odot$ and a young average age of $\sim$40 Myr. Figure 4 shows that the CNR has a radius of $8\rlap.{''}5$, equivalent to 0.42 kpc. According to Buta & Crocker (1993), the CNR has a major axis of $0\rlap.{'}280$, equivalent to a semimajor axis of $8\rlap.{''}40$ or 0.420 kpc. In addition, Comerón et al. (2010) report a CNR with a radius of 0.480 kpc. These values present a much lower dispersion than the previous ones and indicate that the CNR is also located between the iILR (at 0.26 kpc) and the oILR (at 0.90 kpc). The extension of the rotation curve does not allow us to estimate the location of the

OLR. It is also very difficult to determine the end of the spiral arms, since from a radius of $3'$, this galaxy presents very open arms, probably due to interactions, being possible to determine from DSS images an arm $8\rlap.{'}5$ from the center. This galaxy was also observed by the *Hubble Space Telescope* several times in the past. We used UV archive images in the F220W filter[9] to measure the CNR radius and to compare with our measurements. The ring measurement in the F220W filter images gives $R_{CNR} = 7\rlap.{''}7$ in acceptable agreement with our measurements, taking into account the spatial resolution and possible physical spatial differences between different bands.

NGC 2935. This galaxy exhibits some lobesideness in its morphology, and the radial velocity curve is asymmetric (see Figure 2). Florido et al. (2012) observe nonresolved emission and they found knots of gas at large radii, corresponding to H II regions. According to our isophotal fitting from the DSS *R*-band image, this object has an inclination angle of 45°, consistent with previous results (see NED). The rotation curve was fitted considering the southeast part of the radial velocity curve, mainly because of the irregularity that the northwest part presents. The radial velocities of descending values in the range of 1–5 kpc (see Figure 2) are consistent with the detection of a strong incoming flux along the northwestern semimajor axis of the bar. Although the inflow dominates the inner regions on the northwestern side, there is also gas at higher radii with circular velocities with very similar values to those on the southeastern side. Considering that, the fit of only the southeastern side is perfectly representative of the circular velocities of the galaxy.

The two Miyamoto–Nagai fitted components under this assumption give a total mass of $4.3 \times 10^{10} M_\odot$. This object presents a bar with a radial length of $R_{bar} = 24\rlap.{''}3 \pm 0\rlap.{''}7$, equivalent to (3.3 ± 0.1) kpc and we determined that the CR lies at (5.2 ± 0.4) kpc from the galactic nucleus. This yields an $\mathcal{R} = 1.5 \pm 0.2$, indicating that we are in the presence of a slow bar (e.g., Debattista & Sellwood 2000; Rautiainen et al. 2008; Guo et al. 2019). The calculated Ω_p is (26 ± 2) km s^{-1} kpc^{-1} and according to the Hα profile (Figure 4), the CNR has a radius of 0.52 kpc $(3\rlap.{''}77)$, in agreement with Agüero et al. (2016), who report a radius of 0.45 kpc $(3\rlap.{''}26)$. Also, according to (Comerón et al. 2010), the CNR has a semimajor axis of $3\rlap.{''}6$, equivalent to $\sim$0.50 kpc, and Buta & Crocker (1993) measured a CNR diameter of $0\rlap.{'}106$, equivalent to a radius of $3\rlap.{''}18$ and 0.44 kpc. The CNR is confined to a region between the center of the galaxy and the ILR, which is located at 1.2 kpc (see Figure 3). According to our estimation, the OLR is positioned at $\sim$8.3 kpc. The arms, from DSS images, end at $1\rlap.{'}65$ ($\sim$13.56 kpc), away from the OLR. This could be probably due to the high asymmetry commented above that disturbed the galaxy disk. This object, however, presents a particular situation, taking into account what could generate a small variation in Ω_p. On the one hand, there would be no ILR if the pattern speed were increased (see Figure 3). On the other hand, if Ω_p were decreased, there would be two ILRs. In this case, the CNR would be located inside the iILR.

NGC 6753. It is a grand-design spiral galaxy that shows a very pronounced spiral structure (Windhorst et al. 2002). From DSS *R*-band images, our estimation of the major and minor axis gives an inclination angle of 40°, which is in agreement with previous results (see NED). The two Miyamoto–Nagai fitted components give a total mass of $4.2 \times 10^{11} M_\odot$. We

---

9 Proposal ID: 4804, PI: Maoz, Dan.

visually inspect 2MASS images of this galaxy and we do not see any bar, in agreement with Comerón et al. (2010). We estimated the OLR radius by assuming that the spiral arms end before the OLR. With this assumption the OLR is at (14.0 ± 0.8) kpc from the galactic nucleus. This way, the calculated Ω_p in this object is (35 ± 3) km s^{-1} kpc^{-1}. According to our results, the corotation resonance is at (9.4 ± 0.8) kpc. This value is consistent with an obscured region in the vicinity where the spiral arms arise. According to the Hα profile (Figure 4), the CNR radius is $8''50$, equivalent to $\sim$1.89 kpc, in agreement with previous results (Comerón et al. 2010; Agüero et al. 2016). The higher value found in the literature corresponds to a CNR with a diameter of $0'.35$, equivalent to a radius of $10''5$ or 2.16 kpc (Buta & Crocker 1993). Even considering the extreme values, the CNR is located between the iILR (at 0.7 kpc) and the oILR, which is at (2.9 ± 0.2) kpc.

5. Summary and Conclusion

Throughout this work we have studied a sample of five spiral galaxies in order to determine the radii of the CNR and the location of the Lindblad resonances. To carry out this study, we have obtained and analyzed medium resolution spectra in the range of 6200–6900 Å in order to measure the Hα emission line.

Once the radial velocity curves (Figure 2) were determined, we have constructed the rotation curves, to which we fitted two or three components of an axisymmetric Miyamoto–Nagai potential. According to our results, the rotation curves of four of the five galaxies were fitted considering the presence of only two galactic subsystems, i.e., a central ellipsoidal component and a flattened disk. For these objects, it was not necessary to fit an external spherical component (halo). Considering the galaxy IC 1438, three components were fitted to the rotation curve, which are the central ellipsoidal, the flattened disk, and the halo components.

Through the velocity curves fitting, we were able to construct the angular velocity curves and the Lindblad curves. This way, we calculated the location of the Lindblad resonances. In order to measure the circumnuclear radius, we used the Hα emission spatial radial profiles obtained from the 2D observed spectra. For NGC 1512, NGC 2935, and NGC 6753, the obtained values of the CNR radii are in agreement with previous results in the literature. For IC 1438 and IC 4214, the values found in this work show differences of 20% and 10%, respectively, comparing with previous results. Taking into account all the measurements and estimations of the CNR radii, and even considering the extreme values, the CNR are located in all cases between the iILR and the oILR, or between the center and the ILR, as in the case of NGC 2935. This fact is in perfect agreement with previous results (e.g., Buta & Combes 1996; Combes 1996; Sheth et al. 2000; Comerón et al. 2014; Li et al. 2015). Related to this, as we mentioned in Section 4.1, NGC 2935 presents a particular case, considering what would generate a small change in Ω_p. If the pattern speed were increased, it would result in no ILR. On the contrary, if Ω_p were decreased, there would be two ILRs, and the CNR would be located inside the iILR. There are, however, other galaxies studied in the literature which also present only one ILR (e.g., Combes 1996; Shlosman 1999; Comerón et al. 2014).

In summary, although the location of the resonances is known, this information is insufficient to predict the exact radius of the CNR. Although there will be a range of radii where the CNR can be found, it is not enough to know the position of the resonance to know the exact location of the CNR, in agreement with the results of Li et al. (2015). In this scenario, the fact that the CNR are located inside the ILRs is not synonymous to say that the ring formation is due to the ILRs. According to the analysis of Comerón et al. (2010), galaxies with strong bars host smaller rings. In addition, these authors say that galaxies with weak bars can host both larger and smaller nuclear rings. This is in agreement with the results of Kim et al. (2012a), who use hydrodynamic simulations. Recently, Seo et al. (2019) found through 3D simulations that rings are very small when they first form and grow in size over time. These authors found that the size of the CNR depends on the pattern speed, the central mass concentration, and the bar strength. Related to this, Li et al. (2017) suggest that the ring size increases almost linearly with the mass of the central object (e.g., a black hole).

In addition, Li et al. (2015) find through simulations that CNR are in the range of x_2 orbits. Related to this, Regan & Teuben (2003) say that the formation of CNR is more related to x_2 orbits than Lindblad resonances. However, according to some authors, the simulations of the last mentioned work do not have enough resolution to study in detail the structures of gas in the central regions of the galaxy (Li et al. 2015).

All the above considerations, however, are consistent with each other, taking into account that the size and extent of the x_2 orbital family correlate with the location of the inner resonances (e.g., Contopoulos & Grosbol 1989; Athanassoula 1992). In this scenario, the x_2 orbits are in the region confined between the inner resonances.

In this work we showed that different authors, using observations in different bands and with varied spatial and spectral resolutions, obtain similar results in relation with the position of CNR. We have shown that reducing uncertainties in measured parameters hardly brings new elements to the issue of CNR location. Our next step we will delve deeper into the study of the link between the presence of the CNR, the AGN duty cycle, and the life cycle of bars. Placing all these pieces in the same evolutionary scenario represents one of the current challenges in the study of galaxy evolution.

THE ASTRONOMICAL JOURNAL, 158:60 (11pp), 2019 August

Schmidt et al.

ORCID iDs

D. Mast ● https://orcid.org/0000-0003-0469-3193
G. Günthardt ● https://orcid.org/0000-0003-3501-5360
G. Gaspar ● https://orcid.org/0000-0001-9293-4449

References

Agüero, M. P., Díaz, R. J., & Dottori, H. 2016, IJAA, 6, 219
Aguerri, J. A. L., Beckman, J. E., & Prieto, M. 1998, AJ, 116, 2136
Aguerri, J. A. L., Méndez-Abreu, J., Falcón-Barroso, J., et al. 2015, A&A, 576, A102
Arsenault, R. 1989, A&A, 217, 66
Athanassoula, E. 1992, MNRAS, 259, 328
Athanassoula, E., & Misiriotis, A. 2002, MNRAS, 330, 35
Beckman, J. E., Zurita, A., & Vega Beltrán, J. C. 2004, LNEA, 1, 43
Binney, J., & Tremaine, S. 1987, Galactic Dynamics (Princeton, NJ: Princeton Univ. Press)
Böker, T., Falcón-Barroso, J., Schinnerer, E., Knapen, J. H., & Ryder, S. 2008, AJ, 135, 479
Bosma, A. 1978, PhD thesis, Groningen Univ.
Briggs, F. H. 1990, ApJ, 352, 15
Buta, R., & Combes, F. 1996, FCPh, 17, 95
Buta, R., & Crocker, D. A. 1993, AJ, 105, 1344
Buta, R. J., Knapen, J. H., Elmegreen, B. G., et al. 2009, AJ, 137, 4487
Buta, R. J., Sheth, K., Athanassoula, E., et al. 2015, ApJS, 217, 32
Combes, F. 1996, in ASP Conf. Ser. 91, IAU Colloq. 157: Barred Galaxies, ed. R. Buta, D. A. Crocker, & B. G. Elmegreen (San Francisco, CA: ASP), 286
Combes, F. 2001, in Advanced Lectures on the Starburst-AGN, ed. I. Aretxaga, D. Kunth, & R. Mújica (Singapore: World Scientific), 223
Comerón, S., Knapen, J. H., Beckman, J. E., et al. 2010, MNRAS, 402, 2462
Comerón, S., Salo, H., Laurikainen, E., et al. 2014, A&A, 562, A121
Contopoulos, G., & Grosbol, P. 1989, A&ARv, 1, 261
Corbin, M. R. 2000, ApJL, 536, L73
Debattista, V. P., & Sellwood, J. A. 2000, ApJ, 543, 704
Díaz, R. J., Agüero, M. P., & Dottori, H. 2004, arXiv:astro-ph/0409101
Díaz, R. J., Dottori, H., Aguero, M. P., et al. 2006, ApJ, 652, 1122
Díaz, R. J., Dottori, H., Vera-Villamizar, N., & Carranza, G. 2003, ApJ, 597, 860
Doyle, M. T., Drinkwater, M. J., Rohde, D. J., et al. 2005, MNRAS, 361, 34
Elmegreen, D. M. 1998, Galaxies and Galactic Structure (Upper Saddle River, NJ: New Jersey: Prentice Hall)
Ferrarese, L., & Ford, H. 2005, SSRv, 116, 523
Florido, E., Pérez, I., Zurita, A., & Sánchez- Blázquez, P. 2012, A&A, 543, A150
Guo, R., Mao, S., Athanassoula, E., et al. 2019, MNRAS, 482, 1733
Heckman, T. M., González-Delgado, R., Leitherer, C., et al. 1997, ApJ, 482, 114
Ho, L. C., Filippenko, A. V., & Sargent, W. L. W. 1997, ApJ, 487, 591
Hoyle, B., Masters, K. L., Nichol, R. C., et al. 2011, MNRAS, 415, 3627
Hunt, L. K., & Malkan, M. A. 1999, ApJ, 516, 660

Keel, W. C. 1996, ApJS, 106, 27
Kennicutt, R. C., Jr. 1998, ARA&A, 36, 189
Kim, W.-T., Seo, W.-Y., & Kim, Y. 2012a, ApJ, 758, 14
Kim, W.-T., Seo, W.-Y., Stone, J. M., Yoon, D., & Teuben, P. J. 2012b, ApJ, 747, 60
Knapen, J. H. 2005, A&A, 429, 141
Knapen, J. H., Beckman, J. E., Heller, C. H., Shlosman, I., & de Jong, R. S. 1995, ApJ, 454, 623
Kormendy, J. 1979, ApJ, 227, 714
Lauberts, A., & Valentijn, E. A. 1989, The Surface Photometry Catalogue of the ESO-Uppsala Galaxies (Garching: ESO)
Li, Z., Sellwood, J. A., & Shen, J. 2017, ApJ, 850, 67
Li, Z., Shen, J., & Kim, W.-T. 2015, ApJ, 806, 150
Lindblad, B. 1964, ApNr, 9, 103
Ma, C., de Grijs, R., & Ho, L. C. 2017, ApJS, 230, 14
Ma, C., de Grijs, R., & Ho, L. C. 2018, ApJ, 857, 116
Martin, P. 1995, AJ, 109, 2428
Mast, D., Díaz, R. J., & Agüero, M. P. 2006, AJ, 131, 1394
Mast, D., Weidmann, W., Agüero, M. P., et al. 2005, BAAA, 48, 405
Mazzuca, L. M., Swaters, R. A., Knapen, J. H., & Veilleux, S. 2011, ApJ, 739, 104
Merritt, D., & Ferrarese, L. 2001, ApJ, 547, 140
Miyamoto, M., & Nagai, R. 1975, PASJ, 27, 533
Moss, D., Rautiainen, P., & Salo, H. 1999, MNRAS, 303, 125
Piñol-Ferrer, N., Fathi, K., Carignan, C., et al. 2014, MNRAS, 438, 971
Pogge, R. W. 1989, ApJS, 71, 433
Prendergast, K. H. 1983, in IAU Symp. 100, Internal Kinematics and Dynamics of Galaxies, ed. E. Athanassoula (Dordrecht: D. Reidel), 215
Puerari, I., & Dottori, H. 1997, ApJL, 476, L73
Rautiainen, P., Salo, H., & Laurikainen, E. 2008, MNRAS, 388, 1803
Regan, M. W., & Teuben, P. 2003, ApJ, 582, 723
Reshetnikov, V., & Combes, F. 1999, A&AS, 138, 101
Roberts, W. W. J., Huntley, J. M., & van Albada, G. D. 1979, ApJ, 233, 67
Saha, K., de Jong, R., & Holwerda, B. 2009, MNRAS, 396, 409
Saraiva, M. F., Bica, E., Pastoriza, M. G., & Bonatto, C. 2001, A&A, 376, 43
Schmidt, E., Ferreiro, D., Vega Neme, L., & Oio, G. 2016, A&A, 596, A95
Schmidt, E. O. 2019, PASP, 131, 037001
Schmidt, E. O., Oio, G. A., Ferreiro, D., Vega, L., & Weidmann, W. 2018, A&A, 615, A13
Seo, W.-Y., & Kim, W.-T. 2014, ApJ, 792, 47
Seo, W.-Y., Kim, W.-T., Kwak, S., et al. 2019, ApJ, 872, 5
Sheth, K., Regan, M. W., Vogel, S. N., & Teuben, P. J. 2000, ApJ, 532, 221
Shlosman, I. 1999, in ASP Conf. Ser. 187, The Evolution of Galaxies on Cosmological Timescales, ed. J. E. Beckman & T. J. Mahoney (San Francisco, CA: ASP), 100
Shlosman, I., Begelman, M. C., & Frank, J. 1990, Natur, 345, 679
Sofue, Y. 2013, in Mass Distribution and Rotation Curve in the Galaxy, ed. T. D. Oswalt & G. Gilmore (Dordrecht: Springer), 985
Tremaine, S., Gebhardt, K., Bender, R., et al. 2002, ApJ, 574, 740
Van Der Laan, T., Schinnerer, E., Garcia-Burillo, S., et al. 2012, AAS Meeting Abstracts, 219, 323.02
Windhorst, R. A., Taylor, V. A., Jansen, R. A., et al. 2002, ApJS, 143, 113